RSC Advances

PAPER

View Article Online
View Journal | View Issue

Cite this: *RSC Adv.*, 2017, **7**, 50477

The structure and properties of Co substituted $Bi_7Ti_4NbO_{21}$ with intergrowth phases

Changhui Liu,[a] Zezhi Chen,[a] Ranran Peng, *[ab] Zhengping Fu,[ab] Xiaofang Zhai[bc] and Yalin Lu*[abc]

Multiferroic complex oxides with intergrowth aurivillius phases are gaining more and more attention due to the potential to greatly adjust their ferroelectricity (FE) and ferromagnetism (FM) using non-integer layer numbers. In this work, the 2 + 3 aurivillius intergrowth phases of $Bi_7Ti_{4-2x}Co_xNb_{1+x}O_{21}$ were successfully synthesized *via* a solid reaction method. X-ray diffraction (XRD) and high angle annular dark field scanning transmission electron microscopy (HAADF-STEM) analyses clearly demonstrated that Co substituted $Bi_7Ti_{4-2x}Co_xNb_{1+x}O_{21}$ keeps an intergrowth phase structure when $x \leq 0.3$. A new analysis method that maps the linear brightness in HAADF images was used to give the clear Bi atom position, and this revealed that the lattice shrinkage in the *c* direction caused by Co substitution mainly occurred at the $(BiTiNbO_7)^{2-}$ block in the (Bi_3TiNbO_9) layer, which was also confirmed by an investigation using Raman spectroscopy. Polarization–electric field (*P*–*E*) investigations and pulsed polarization positive-up negative-down (PUND) measurements indicated that $Bi_7Ti_{4-2x}Co_xNb_{1+x}O_{21}$ (x = 0.1, 0.2, and 0.3) presents much enhanced properties compared with non-substituted $Bi_7Ti_4NbO_{21}$. For example, $2E_c$ = 135.23 kV cm^{-1} and $2P_r$ = 9.33 μC cm^{-2} can be achieved when x = 0.3. Also with Co substitution, $Bi_7Ti_4NbO_{21}$ changed from diamagnetic (χ < 0) to paramagnetic ($\chi \approx 7 \times 10^{-5}$). The calculated effective magnetic moments in the $Bi_7Ti_{4-2x}Co_xNb_{1+x}O_{21}$ samples have similar values, suggesting that the cobalt atoms in the materials have almost the same efficient moment.

Received 22nd September 2017
Accepted 16th October 2017

DOI: 10.1039/c7ra10522c

rsc.li/rsc-advances

Introduction

Ferroelectric and/or ferromagnetic co-existing layered bismuth complex oxides with an aurivillius structure (LBOA) have recently been attracting considerable interest because of their amazing layered crystalline structures, valuable coupled physical properties, and potential applications in multiple-state storage, transducers, amplitude modulators, and optical wave devices.[1–9] Normally, the crystalline structures of LBOAs can be generally formulated as $(Bi_2O_2)^{2+}(A_{m-1}B_mO_{3m+1})^{2-}$ in which the $(Bi_2O_2)^{2+}$ fluorite-type layers alternate with $(A_{m-1}B_mO_{3m+1})^{2-}$ perovskite slabs, where A is a mono-, di-, or tri-valent ion, such as Na^+, K^+, Pb^{2+}, Ba^{2+}, Sr^{2+}, Bi^{3+}, or a mixture of them; B represents a small sized cation with tetra-, penta-, or hexa-valence, such as Ti^{4+}, Nb^{5+}, Ta^{5+}, or W^{6+}; and *m*, usually an integer, is the number of mono-octahedral layers between the $(Bi_2O_2)^{2+}$ layers.[10] As their crystalline structures, chemical stability, as well as dielectric and ferroelectric properties can be affected by *m*, the intergrowth of LBOA compounds with two constituent structures (generally *m* and *m* + 1) alternating along the common *c*-axis, such as Bi_2WO_6–Bi_3TiNbO_9, Bi_3TiNbO_9–$Bi_4Ti_3O_{12}$, and $Bi_4Ti_3O_{12}$–$Bi_5Ti_3FeO_{15}$,[10–19] was designed and synthesized to enable further tailoring of their properties. It is generally believed that these compounds with intergrowth aurivillius phases show better properties compared with non-intergrowth LBOAs. For example, the remanent polarization ($2P_r$) of Bi_3TiNbO_9–$Bi_4Ti_3O_{12}$ is ~20.1 μC cm^{-2} at 423 K, much larger than the values of Bi_3TiNbO_9 (~11 μC cm^{-2}) and $Bi_4Ti_3O_{12}$ (~16 μC cm^{-2}).[10] In general, the majority of such materials investigated before were ferroelectric.

In the ferroelectric Bi_3TiNbO_9–$Bi_4Ti_3O_{12}$ ($Bi_7Ti_4NbO_{21}$) system shown in Fig. 1, for example, 3-layered $(Bi_2Ti_3O_{10})^{2-}$ and 2-layered $(BiTiNbO_7)^{2-}$ arrange alternately between the neighbouring $(Bi_2O_2)^{2+}$ layers. The theoretical and property studies of these amazing structures of $Bi_7Ti_4NbO_{21}$ have attracted much attention.[10,12] Moreover, to intensively modulate the properties of $Bi_7Ti_4NbO_{21}$, many types of A-site substitution, such as La, W, Er and Na, were adapted, and the properties of some of these were obviously improved.[12,14,16,18,19] Unfortunately, although it may trigger another regulating factor in the properties, substituting the magnetic ions in the B-sites to generate a multiferroic has rarely been studied in the intergrowth of $Bi_7Ti_4NbO_{21}$.

[a]*CAS Key Laboratory of Materials for Energy Conversion, Department of Materials Science and Engineering, University of Science and Technology of China, Hefei 230026, P. R. China. E-mail: yllu@ustc.edu.cn; pengrr@ustc.edu.cn*

[b]*Synergetic Innovation Center of Quantum Information & Quantum Physics, University of Science and Technology of China, Hefei, Anhui 230026, China*

[c]*National Synchrotron Radiation Laboratory, University of Science and Technology of China, Hefei 230026, PR China*

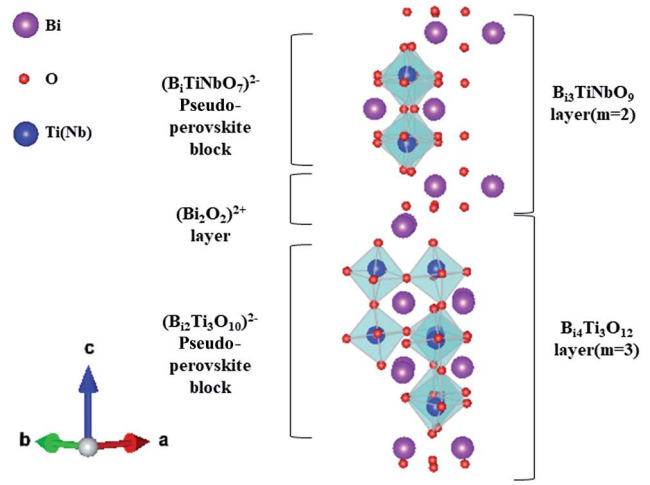

Fig. 1 A schematic representation of the crystalline structure of $Bi_7Ti_4NbO_{21}$.

In this work, $Bi_7Ti_{4-2x}Co_xNb_{1+x}O_{21}$ ($x = 0$, 0.1, 0.2, 0.3, and 0.4) specimens were successfully synthesized *via* a solid state reaction. The amounts of the Ti and Nb ions changed simultaneously with Co substitution to keep the charge balance. The effect of Co substitution on the structure of $Bi_7Ti_{4-2x}Co_xNb_{1+x}O_{21}$ was investigated in detail, and the ferroelectric and ferromagnetic properties of $Bi_7Ti_{4-2x}Co_xNb_{1+x}O_{21}$ were also studied as functions of the Co content.

Experimental section

Polycrystalline Co-substituted $Bi_7Ti_4NbO_{21}$ powders were prepared *via* a conventional solid-state reaction. Appropriate amounts of Bi_2O_3 (99.99% purity, Jiangsu Gold Wall Reagent Co., China), TiO_2 (99.71% purity, Sinopharm Chemical Reagent Co., China), Nb_2O_5 (99.5% purity, Sinapharm Chemical Reagent Co., China), and Co_2O_3 (99.98% purity, Jiangsu Gold Wall Reagent Co., China) were mixed in an agate jar, blending with agate balls for more than 24 hours in ethanol. An excess of 5 mol% Bi_2O_3 was used to compensate for the volatilization of bismuth oxide during the calcination process. After drying at 70 °C for 24 h, the milled powders were heated at 900 °C for 7 h. To fabricate ceramic pellets, the $Bi_7Ti_4NbO_{21}$ powders were cold-pressed into disks that were 12 mm in diameter and 0.9 mm thick at a pressure of 150 MPa, and then sintered at 1180 °C for 4 h in air to prepare dense $Bi_7Ti_{4-2x}Co_xNb_{1+x}O_{21}$ ceramics.

The crystalline structures of the $Bi_7Ti_{4-2x}Co_xNb_{1+x}O_{21}$ samples were investigated using powder X-ray diffraction (XRD) with Cu-Kα radiation (TTR-III, Japan). The atomic structures of the samples were visualized using high angle annular dark field aberration corrected scanning transmission electron microscopy (HAADF-STEM, JEM-ARM200F, JEOL, Japan). The microstructures of the fractured samples were observed using scanning electron microscopy (SEM) (JEOL, JSM-6400). Raman spectra were obtained with a SPEX-1403 Laser Raman spectrometer using a 514.5 nm Ar+ laser as an excitation source (LabRamHR, France). For the ferroelectric and dielectric measurements, the pellets were polished to about 0.3 mm in thickness, and then Ag was evaporated on both of the surfaces, which would act as electrodes. Ferroelectric measurements were conducted using a Precision LC ferroelectric analyzer at an applied frequency of 50 Hz (Radiant Technology, USA). The magnetic properties of the samples were characterized by a vibrating sample magnetometer option of the Quantum Design physical property measurement system (PPMS-VSM, Quantum Design, USA).

Results and discussion

XRD and HAADF-STEM

Fig. 2(a) shows the room-temperature XRD patterns of the $Bi_7Ti_{4-2x}Nb_{1+x}Co_xO_{21}$ ($x = 0$, 0.1, 0.2, 0.3, and 0.4) pellets sintered at 1180 °C. When $x \leq 0.3$, all the XRD diffraction peaks match well to those of $Bi_7Ti_4NbO_{21}$with a space group symmetry of *I2cm*,[10] indicating that no secondary phase was detected, whereas the Bi_3TiNbO_9 phase precipitated when x was set as 0.4. Therefore, in this work, to eliminate the effects from impurities, the properties of $Bi_7Ti_{4-2x}Nb_{1+x}Co_xO_{21}$ (BTNC) were studied when $x \leq 0.3$.

Enlarged views of the XRD spectra near the main peak (018) are shown in Fig. 2(b) for the BTNC samples ($x \leq 0.3$). It can be clearly seen that the main peak shifts toward the higher angle when increasing the Co content, indicating the reduced lattice parameter c. Rietveld refinements of the XRD patterns were performed with the Material Studio 6.0 program and the refined cell parameters are listed in Table 1 and also shown in Fig. 2(c) as a function of the Co content. It can be clearly seen that all the lattice parameters reduce with an increase of the Co content. Considering the ionic radii of Co^{3+} (54.5 pm), Nb^{5+} (64.0 pm) and Ti^{4+} (60.5 pm), the shrinkage of the lattice parameters should result from the smaller average radius of Co^{3+} and Nb^{5+} (59.25 pm), which are substituted as a pair to keep the charge balance.

To illustrate the formation process for its 2 + 3 intergrowth structure, the crystalline structures of $Bi_7Ti_{3.6}Co_{0.2}Nb_{1.2}O_{21}$ powders calcined at different temperatures were also investigated. As shown in Fig. 2(d), when calcined at 900 °C, the spectra corresponding to Bi_3TiNbO_9, $Bi_4Ti_3O_{12}$ and $Bi_7Ti_4NbO_{21}$ based oxides can be clearly identified. With the enhancement of the calcination temperatures, the peaks corresponding to Bi_3TiNbO_9 and $Bi_4Ti_3O_{12}$ recede and become invisible when calcined at 1180 °C, suggesting that Bi_3TiNbO_9 and $Bi_4Ti_3O_{12}$ based oxides react to form $Bi_7Ti_4NbO_{21}$ based complex oxides. It should be noted that the detailed formation procedure for how Bi_3TiNbO_9 inserts into the $Bi_4Ti_3O_{12}$ lattice (or inverse) to form Co substituted $Bi_7Ti_4NbO_{21}$ is still unclear and needs intensive investigation.

The HAADF-STEM images of the $Bi_7Ti_{4-2x}Co_xNb_{1+x}O_{21}$ powders ($x = 0$ and 0.2) are shown in Fig. 3. It is well known that the brightness of the atoms in the HAADF-STEM images depends on the atomic number. Therefore, the spots representing the Bi atoms are much brighter than those representing all the other atoms. As shown in Fig. 3(a), 2 and 3 layers of the Bi

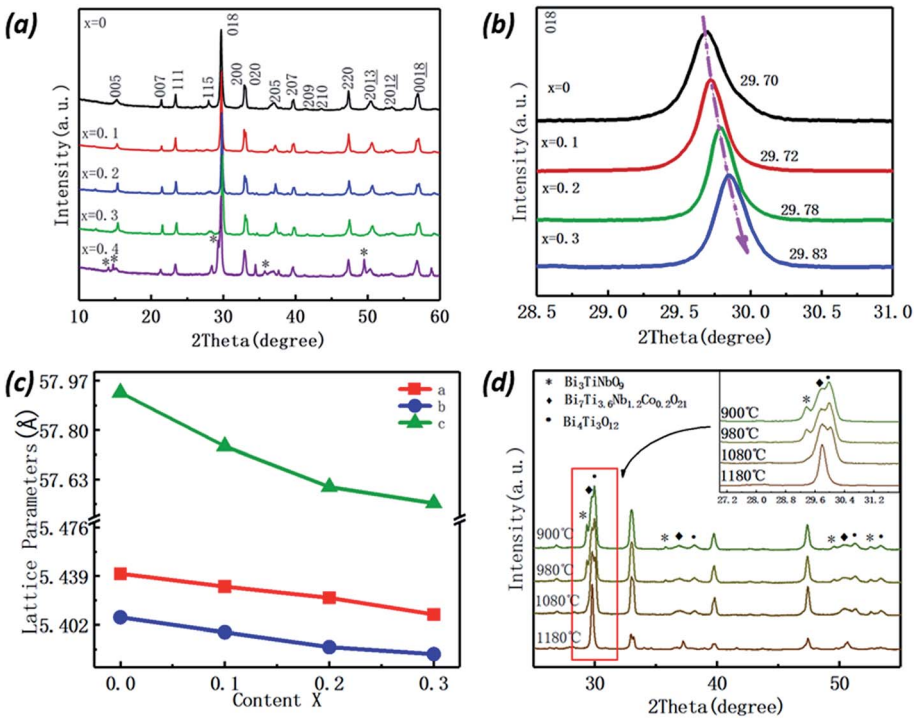

Fig. 2 (a) The RT XRD patterns of $Bi_7Ti_{4-2x}Co_xNb_{1+x}O_{21}$ ($x = 0$, 0.1, 0.2, 0.3, and 0.4). (b) The magnified sections of the XRD patterns in the 2θ range of 28.5–31.0°. (c) The refined lattice parameters *vs.* the Co content in $Bi_7Ti_{4-2x}Co_xNb_{1+x}O_{21}$ ($x = 0$, 0.1, 0.2, and 0.3). (d) The XRD patterns of the $Bi_7Ti_{3.6}Co_{0.2}Nb_{1.2}O_{21}$ powders calcined at different temperatures.

Table 1 The refined lattice parameters of $Bi_7Ti_{4-2x}Co_xNb_{1+x}O_{21}$ ($x = 0$, 0.1, 0.2, and 0.3)

	Lattice parameter (Å)					
x	a	b	c	Unit cell volume (Å^3)	R_{wp}	R_p
0	5.4408 (3)	5.4076 (7)	57.9292 (31)	1704.40 (71)	8.26%	15.35%
0.1	5.4309 (8)	5.3964 (1)	57.7439 (70)	1692.34 (91)	8.78%	18.44%
0.2	5.4224 (7)	5.3852 (1)	57.6039 (00)	1682.10 (20)	9.64%	19.91%
0.3	5.4098 (7)	5.3798 (9)	57.5475 (79)	1680.71 (60)	9.43%	18.37%
Bi_3TiNbO_9 (ref. 20)	5.4394	5.3985	25.13			
$Bi_4Ti_3O_{12}$ (ref. 16)	5.45	5.41	32.84			

atoms (bright spots) are sandwiched by two closely stacked Bi layers, which present in an orderly and alternating manner, indicating the intergrowth of the two pseudo-perovskite blocks (as indicated in Fig. 1).

To indicate the substitution effect on the atomic structure, enlarged views of the HAADF-STEM images for the $x = 0$ and $x = 0.2$ samples are shown in Fig. 3(b) and (c), respectively.[33] To this end, a new method to map the brightness scanned along two lines (indicated in the images) is applied to give the clear Bi atom positions. Shown in Fig. 3(b), line 1 (along the c direction) in the $Bi_7Ti_4NbO_{21}$ sample starts from the Bi atom in the $(Bi_2O_2)^{2+}$ layer and passes through the Bi atoms in the $(Bi_2Ti_3O_{10})^{2-}$ block (indicated in Fig. 1); yet, when entering the neighbouring $(Bi_2O_2)^{2+}$ layer, line 1 goes between the two adjacent Bi ions caused by the shifted position of Bi in the $[Bi_2O_2]^{2+}$ layer, which makes line 1 pass through the dark spots corresponding to the B site ions, such as Ti, Nb, and Co atoms, in the following $(BiTiNbO_7)^{2-}$ block, and therefore, the brightness corresponding to line 1 presents 4 strong peaks and then two weak peaks. It should be noted that the two Bi ions in $[Bi_2O_2]^{2+}$ only present one peak with a small tail caused by the shifted position of the neighbouring Bi ions. From the peak position along the line, the layer distance in each block can be calculated as $c/2 \approx 2.899$ nm, very close to the simulated value of c ($c/2 = 5.79292/2 \approx 2.8965$ nm). Importantly, the Bi–Bi distance in the $Bi_4Ti_3O_{12}$ layer is found to show great dependence on the positions, suggesting different lengths of the oxygen octahedral along the c direction. As shown in Fig. 3(b), the lengths of the oxygen octahedral are about 0.471 when located close to the $(Bi_2O_2)^{2+}$ layer and 0.422 nm when located in the centre of the $(Bi_2Ti_3O_{10})^{2-}$ block.

Similarly, line 2 starts from the $(Bi_2O_2)^{2+}$ layer and goes between the Bi atoms in the $(Bi_2Ti_3O_{10})^{2-}$ block and passing through the Bi atoms in the neighbouring $(Bi_2Ti_3O_{10})^{2-}$ block

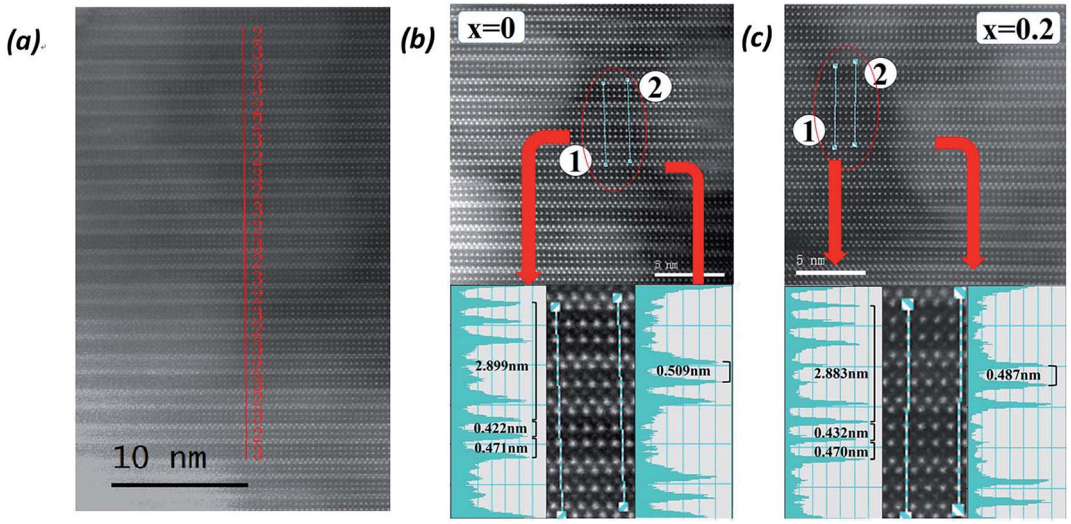

Fig. 3 (a) The HAADF-STEM image of the $Bi_7Ti_{3.6}Nb_{1.2x}Co_{0.2}O_{21}$ ceramic specimen; (b) the STEM image of the $Bi_7Ti_4NbO_{21}$ ($x = 0$) sample along with its brightness map scanned at lines 1 and 2; (c) the STEM image of the $Bi_7Ti_{3.6}Nb_{1.2x}Co_{0.2}O_{21}$ ($x = 0.2$) sample and its brightness map scanned at lines 1 and 2.

caused position shifts of Bi^{3+} in the $(Bi_2O_2)^{2+}$ layer. Accordingly, the brightness of line 2 presents four weak peaks at first and then three strong peaks. Therefore, the Bi–Bi distance in the *c* axis can be measured as 0.509 nm in the $(BiTiNbO_7)^{2-}$ block, indicating a much longer oxygen octahedral along the *c* direction than that in the $(Bi_2Ti_3O_{10})^{2-}$ block.

While for $Bi_7Ti_{3.6}Co_{0.2}Nb_{1.2}O_{21}$, the Bi–Bi distances in the *c* axis can be measured as 0.487 nm in the $(BiTiNbO_7)^{2-}$ based block and 0.470 and 0.432 nm in the $(Bi_2Ti_3O_{10})^{2-}$ based block, respectively, illustrated in Fig. 3(c). Compared to $Bi_7Ti_4NbO_{21}$, the main change in the Bi–Bi distance occurs in the $(BiTiNbO_7)^{2-}$ block, shrinking from 0.509 to 0.487 nm. This result seems to imply that Co with an ionic radius of 54.5 pm mainly incorporates into the $(BiTiNbO_7)^{2-}$ block. One thing to be noted is that the value of $c/2$ measured in Fig. 3(c) is 2.883 nm for $Bi_7Ti_{3.6}Co_{0.2}Nb_{1.2}O_{21}$, very close to that simulated from the XRD spectra ($c/2 \approx 2.8802$ nm). This result further indicates the credibility of this brightness map method.

Raman analysis

Raman spectroscopy was used to investigate the Co substitution effect on the structure of $Bi_7Ti_4NbO_{21}$. As shown in Fig. 4, for $Bi_7Ti_4NbO_{21}$ ($x = 0$), the Raman modes at 117, 234, 267, 323, 356, 530, 573, 815 and 865 cm^{-1} can be clearly observed. Previous studies[11,21,31,32] indicated that the bands below 200 cm^{-1} should originate from the vibration of the heavy mass Bi^{3+} ions, and the bands above 200 cm^{-1} are ascribed to the TiO_6 and NbO_6 octahedrals.[23,29] Therefore, the 117 cm^{-1} bands should result from the vibration of the Bi^{3+} ions at the A-sites in the perovskite-like layer;[23]the modes at 234 and 267 cm^{-1} represent the twisting vibrations of the O–Ti–O or O–(Ti, Nb)–O structures; the 323 and 356 cm^{-1} modes correspond to the different directions of the O–Ti–O or O–(Ti, Nb)–O bending in the *a*–*b* plane;[24,28] the modes located at 530 and 573 cm^{-1} [21] are attributed to the relative vibration of the O atoms at the top of the TiO_6 octahedral; and the bands at 815 and 865 cm^{-1} represent the symmetric stretching of the (Ti, Nb)O_6 and TiO_6 octahedrals, respectively.[11,24,28–30]

For the Co-doped specimens, the Raman spectra have similar shapes to that of $Bi_7Ti_4NbO_{21}$, of which the original peaks still exist in spite of the little peak shifts or intensity changes. A new mode at 726 cm^{-1} appears and increases substantially with the increase of the Co content in the $Bi_7Ti_{4-2x}Co_xNb_{1+x}O_{21}$ samples. This mode may be caused by the vibration of the CoO_6 octahedra, which can be observed in the Raman spectra of $LaCoO_3$ and $La_{0.8}Sr_{0.2}CoO_3$. This result clearly indicates that the Co ions have entered the perovskite slab.[22] It should also be noted that the two modes above 800 cm^{-1} show different dependence on the Co substitution: the mode at 815 cm^{-1} shifts to higher frequency, while the mode at 865 cm^{-1} does not shift obviously. This result may suggest that cobalt substitution in the specimens mainly impacts the (Ti, Nb)O_6 octahedral in the $[Bi_3TiNbO_9]$ layer instead of the TiO_6

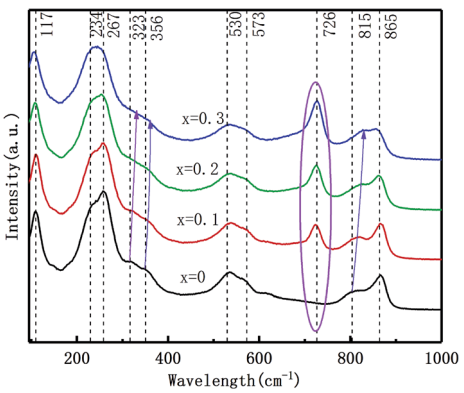

Fig. 4 The Raman spectra of $Bi_7Ti_{4-2x}Co_xNb_{1+x}O_{21}$.

octahedral in the $Bi_4Ti_3O_{12}$ lattice. This result is in good agreement with the HAADF-STEM image analysis.

The SEM results of $Bi_7Ti_{4-2x}Nb_{1+x}Co_xO_{21}$ ($x = 0$, 0.1, 0.2, and 0.3) are shown in Fig. 5. It can clearly be seen that all the samples are dense and suitable for later ferroelectric and ferromagnetic study.

Ferroelectric properties

The room-temperature polarization–electric field (P–E) hysteresis loops of all the $Bi_7Ti_{4-2x}Co_xNb_{1+x}O_{21}$ samples are shown in Fig. 6(a), and the resulting remanent polarization ($2P_r$) and coercive field ($2E_c$) measured under a field of 150 kV cm^{-1} are shown in Fig. 6(b) as a function of the Co content (x) in the samples.

Measured at 150 kV cm^{-1}, the remanent polarization ($2P_r$) of $x = 0$ is ~2.57 μC cm^{-2}, which has good consistency with the previous report.[34] As shown in Fig. 6(b), with the increase of the Co content, both $2P_r$ and the coercive fields ($2E_c$) increase sharply first, then slowly, and reach about 9.33 μC cm^{-2} and 135.23 kV cm^{-1} for $x = 0.3$, larger than those of $Bi_{5.5}Nd_{1.5}Ti_4NbO_{21}$ ($2P_r \sim 8$ μC cm^{-2} and $2E_c \sim 90$ kV cm^{-1}).[34]

To exclude a possible artificial polarization from the contribution of leakage current, pulsed polarization positive-up negative-down (PUND) measurements were performed and the results are shown in Fig. 6(c). The pulsed remanent polarizations ΔP (switched polarization − non-switched polarization) of the samples have similar Co-content (x) dependence with $2P_r$ determined from the P–E loops (shown in Fig. 6(d)). Measured at 150 kV cm^{-1}, the values of ΔP are 2.42 and 6.98 μC cm^{-2} for $x = 0$ and $x = 0.2$, respectively, in good accordance with those values of $2P_r$. This result indicates that the polarization of the samples arises mainly from the intrinsic materials and rarely from leakage current contributions.[25,26] As a result of this, the increase of the $2P_r$ value with cobalt incorporation should be attributed to the structural evolution (lattice shrinkage). As indicated in Table 1, with Co substitution in Bi_3TiNbO_9–$Bi_4Ti_3O_{12}$, the lattice of $Bi_7Ti_{4-2x}Nb_{1+x}Co_xO_{21}$ shrinks greatly, to have much lower lattice parameters than those of pure Bi_3TiNbO_9 (ref. 20) and $Bi_4Ti_3O_{12}$.[16] Considering that Co is mainly incorporated into the (Bi_3TiNbO_9) layer, a large amount of tension will be applied to the ($Bi_4Ti_3O_{12}$) layer to make the lattice shrink accordingly. This will introduce large lattice distortion and should be the main reason for the observed enlarged values of P_r and E_c in the ferroelectric measurements.

Magnetic properties

Fig. 7(a) shows the magnetic hysteresis loops of the $Bi_7Ti_{4-2x}Co_xNb_{1+x}O_{21}$ ($x = 0$, 0.1, 0.2, 0.3) ceramics measured at 10 K. When $x = 0$, a diamagnetism characteristic is observed; while in the case of the Co-doped specimens, the loops show magnetic nature, which increases with the Co content. The temperature dependence of magnetization for the $Bi_7Ti_{4-2x}Co_xNb_{1+x}O_{21}$ ($x =$ 0, 0.1, 0.2, and 0.3) samples is shown in Fig. 7(b). It can be clearly seen that the magnetic moment increased with the heavily Co doped samples. There was no phase transition or glass state appearing within the measured temperature range.

To get more information about the magnetic properties of the Co-doped specimens, we use the Curie–Weiss law to explore the magnetic interaction and effective magnetic moment (M_{eff}) of the samples.[25–27] According to the Curie–Weiss law, the magnetic susceptibility (χ) of a paramagnetic substance complies with the following formula (1):

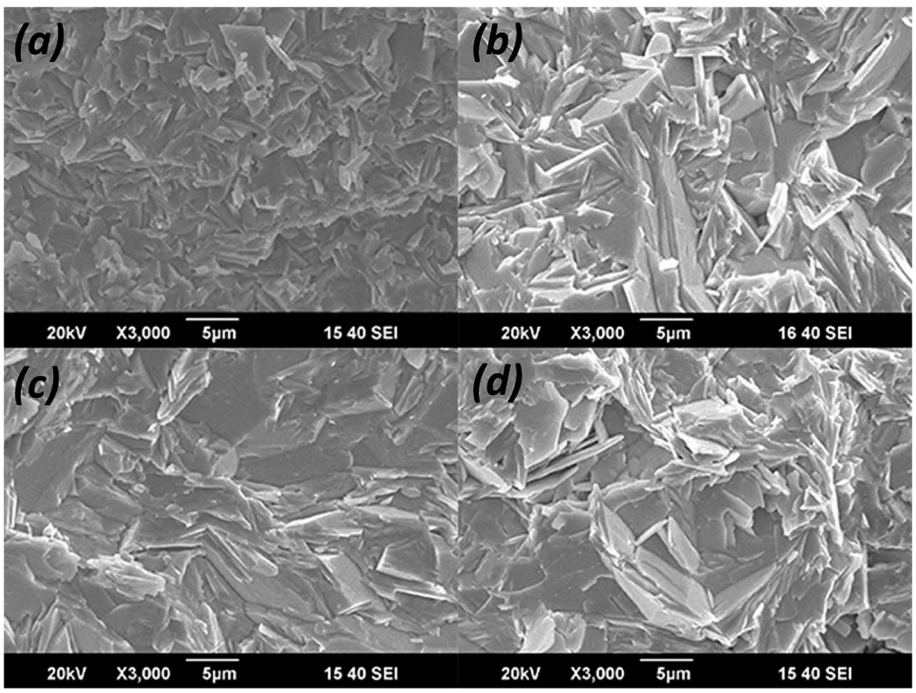

Fig. 5 The fractured microstructure of $Bi_7Ti_{4-2x}Nb_{1+x}Co_xO_{21}$ with (a) $x = 0$, (b) $x = 0.1$, (c) $x = 0.2$, and (d) $x = 0.3$.

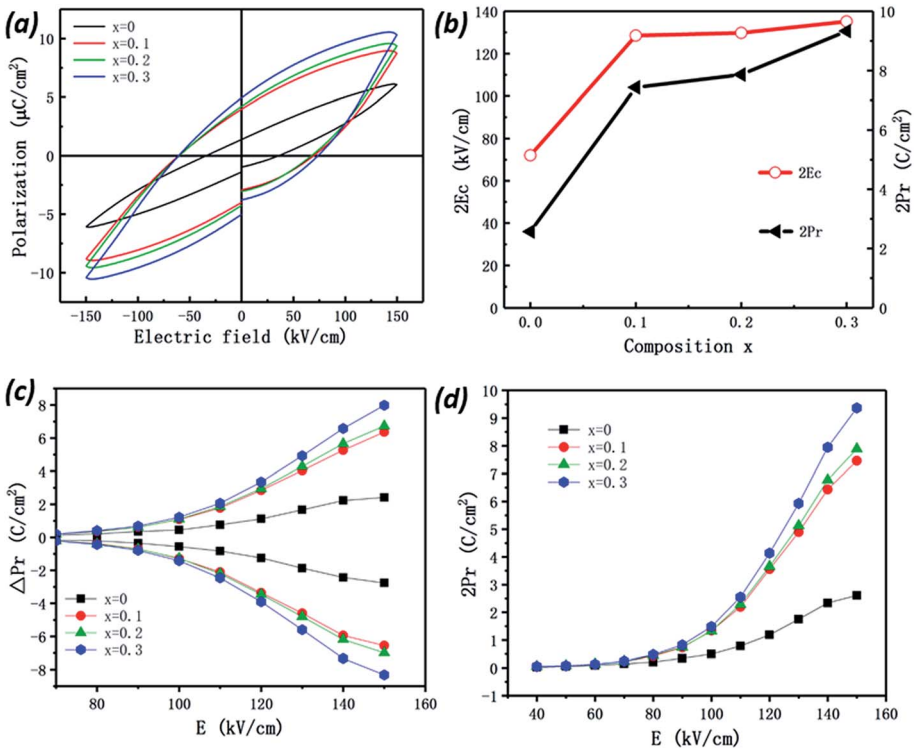

Fig. 6 (a) The P–E hysteresis loops of $Bi_7Ti_{4-2x}Co_xNb_{1+x}O_{21}$ ($x = 0$, 0.1, 0.2, and 0.3) at 150 kV cm^{-1}; (b) the dependence of $2E_c$ and $2P_r$ on the Co content (x); and ΔP (c) and $2P_r$ (d) of $Bi_7Ti_{4-2x}Co_xNb_{1+x}O_{21}$ ($x = 0$, 0.1, 0.2, and 0.3) measured in different electrical fields.

$$\chi = \frac{c}{T + \Theta_c} \quad (1)$$

$$\frac{1}{\chi} = \frac{1}{c}T + \frac{c}{\Theta_c} \quad (2)$$

where χ, c, T, and Θ_c represent the magnetic susceptibility, Curie–Weiss constant ($c > 0$), temperature and Curie point, respectively. So, the values of $1/\chi$ and T have a linear relationship, shown in eqn (2). We fit the $1/\chi$–T curves of all the samples, as shown in Fig. 7, and then the slope ($1/c$) can be calculated from the linear dependence about $1/\chi$ and T. The Curie–Weiss constant (c) can also be regarded as a function of the spin angular momentum (S), as shown in eqn (3).

$$c = \frac{Ng^2\mu_B{}^2 S(S+1)}{3k_B} \quad (3)$$

where empirical constant $g = 2$; μ_B and k_B indicate the Bohr magnon and Boltzmann constants, respectively; and N indicates the number of cobalt atoms in each cell ($N = 0.1$, 0.2, and 0.3).

The effective magnetic moment is the function of the spin angular momentum and therefore can be related to the Curie–Weiss constant, as shown in eqn (4):

$$M_{\text{eff}} = g\mu_B\sqrt{S(S+1)} = \sqrt{\frac{3k_Bc}{Ng\mu_B}} = \sqrt{\frac{3k_B}{g\mu_B}} \times \sqrt{\frac{c}{N}} \quad (4)$$

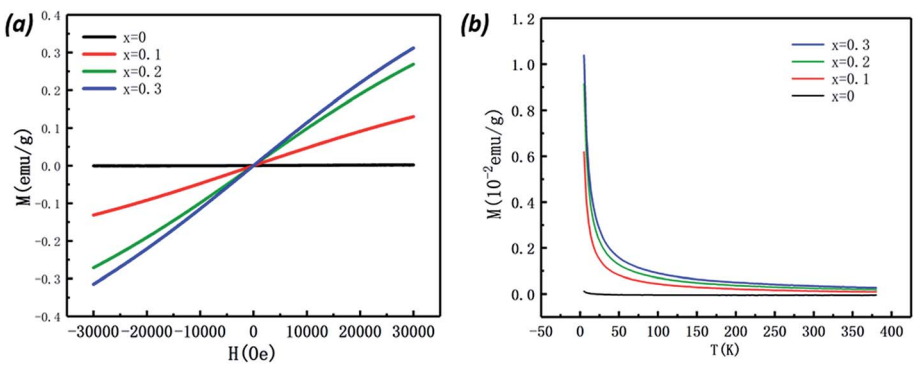

Fig. 7 (a) The magnetic hysteresis loops of the $Bi_7Ti_{4-2x}Co_xNb_{1+x}O_{21}$ ($x = 0$, 0.1, 0.2, and 0.3) ceramics at 10 K. (b) The temperature dependence of magnetization of the samples in the ZFC–FC modes measured at 500 Oe.

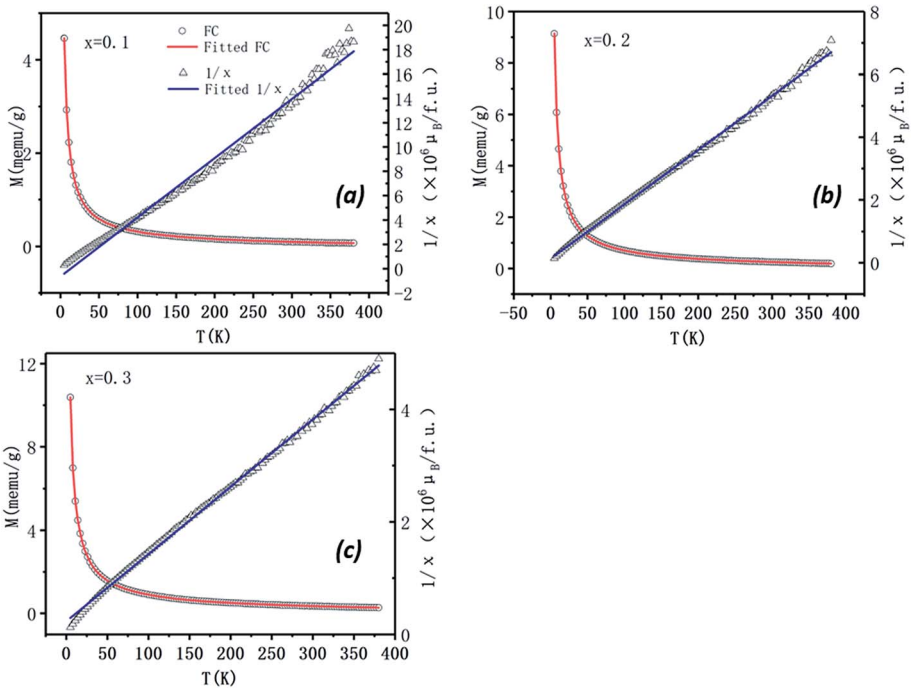

Fig. 8 The temperature dependence of magnetization of $Bi_7Ti_{4-2x}Co_xNb_{1+x}O_{21}$ with $x = 0.1$ (a), 0.2 (b), and 0.3 (c) measured in the FC modes at 500 Oe. The relevant inverse magnetic susceptibility ($1/\chi$) *versus* temperature (T) in the FC mode and the fitted curves (blue line) according to the Curie–Weiss Law for the sample are also present.

According to Fig. 8 the effective magnetic moment can be calculated as 1.12 μ_B, 1.12 μ_B, and 1.14 μ_B in the $x = 0.1$, 0.2, and 0.3 specimens, respectively. The similar M_{eff} values suggest that the cobalt atoms in the materials have almost the same efficient moment in those samples.

Conclusions

(1) Co atoms can be a substitution for Ti atoms in the $Bi_7Ti_4NbO_{21}$ lattice without destroying the structure.

(2) Because of the different radii of the Co, Nb and Ti ions, the lattice of the 2 + 3 intergrowth aurivillius complex oxide shrinks after Co insertion, which mainly occurs in the $(BiTiNbO_7)^{2-}$ slab.

(3) The ferroelectric properties of Co substituted $Bi_7Ti_4NbO_{21}$ improve dramatically, with $2P_r$ increasing from 2.57 μC cm^{-2} ($x = 0$) to more than 9.33 μC cm^{-2} ($x = 0.3$).

(4) The original $Bi_7TI_4NbO_{21}$ was a diamagnetic compound. With Co substitution, $Bi_7Ti_{4-2x}Co_xNb_{1+x}O_{21}$ (x = 0.1, 0.2, and 0.3) presents paramagnetic property.

Conflicts of interest

There are no conflicts to declare.

Acknowledgements

This work was supported by the National Key R&D Program of China (2016YFA0401004), the Chinese Universities Scientific Fund (CUSF, WK2310000055), the Anhui Provincial Natural Science Foundation (P. R. China, No. 1608085QE91), and the External Cooperation Program of BIC (Chinese Academy of Sciences, No. 211134KYSB20130017).

References

1 Y. Moritomo, A. Asamitsu, H. Kuwahara and Y. Tokura, *Nature*, 1996, **380**, 141–144.
2 M. Fiebig, *J. Phys. D: Appl. Phys.*, 2005, **38**, R123–R152.
3 K. F. Wang, J. M. Liu and Z. F. Ren, *Adv. Phys.*, 2009, **58**, 321–448.
4 N. A. Spaldin, S.-W. Cheong and R. Ramesh, *Phys. Today*, 2010, **63**, 38–43.
5 S. Ikegami and I. Ueda, *Jpn. J. Appl. Phys.*, 1974, **13**, 1572–1577.
6 B. Park, B. Kang, S. Bu, T. Noh, J. Lee and W. Jo, *Nature*, 1999, **401**, 682–684.
7 M. Maeder, D. Damjanovic and N. Setter, *J. Electroceram.*, 2004, **13**, 385–392.
8 T. Takenaka and H. Nagata, *J. Eur. Ceram. Soc.*, 2005, **25**, 2693–2700.
9 S. Zhang, F. Yu and D. J. Green, *J. Am. Ceram. Soc.*, 2011, **94**, 3153–3170.
10 Z. G. Yi, Y. Wang, Y. X. Li and Q. R. Yin, *J. Appl. Phys.*, 2006, **99**, 114101.
11 W. Wang, S.-P. Gu, X.-Y. Mao and X.-B. Chen, *J. Appl. Phys.*, 2007, **102**, 024102.
12 X. Gao, H. Gu, Y. X. Li, Z. G. Yi, M. Čeh and K. Žagar, *J. Mater. Sci.*, 2011, **46**, 5423–5431.

13 Z. G. Yi, Y. X. Li, Q. B. Yang and Q. R. Yin, *Ceram. Int.*, 2008, **34**, 735–739.
14 H. Ogawa, D. Iida, S. Takahashi, T. Moriyama and A. Kan, *Ferroelectrics*, 2016, **498**, 1–11.
15 L. Fei, Z. Zhou, S. Hui and X. Dong, *Ceram. Int.*, 2015, **41**, 9729–9733.
16 X. Tian, S. Qu, B. Wang, H. Du and Z. Xu, *J. Inorg. Organomet. Polym. Mater.*, 2013, **24**, 355–359.
17 S. Nakashima, H. Fujisawa, S. Ichikawa, J. M. Park, T. Kanashima, M. Okuyama and M. Shimizu, *J. Appl. Phys.*, 2010, **108**, 074106.
18 H. Zhang, H. Yan and M. J. Reece, *J. Appl. Phys.*, 2010, **107**, 104111.
19 H. Zou, J. Li, Q. Cao, X. Wang, X. Hui, Y. Li, Y. Yu and X. Yao, *J. Adv. Dielectr.*, 2014, **04**, 1450028.
20 Z. Zhang, H. Yan, X. Dong and Y. Wang, *Mater. Res. Bull.*, 2003, **38**, 241–248.
21 Y. L. Du, M. S. Zhang, Q. Chen, Z. R. Yuan, Z. Yin and Q. A. Zhang, *Solid State Commun.*, 2002, **124**, 113–118.
22 X. Li, Z. Y. Peng, W. Fan, K. Guo, J. M. Gu, M. Y. Zhao and J. F. Meng, *Mater. Chem. Phys.*, 1996, **46**, 50–54.
23 J. Zhu, X.-Y. Mao and X.-B. Chen, *Acta Phys. Sin.*, 2004, **53**, 3929–3933.
24 J. Zhu, X.-B. Chen, J.-h. He and J.-C. Shen, *Phys. Lett. A*, 2007, **362**, 471–475.
25 Y. Huang, S. Sun, G. Wang, J. Wang, R. Peng and Y. Lu, *RSC Adv.*, 2014, **4**, 29264.
26 J. Wang, L. Li, R. Peng, Z. Fu, M. Liu, Y. Lu and X. Tan, *J. Am. Ceram. Soc.*, 2015, **98**, 1528–1535.
27 D. L. Zhang, W. C. Huang, Z. W. Chen, W. B. Zhao, L. Feng, M. Li, Y. W. Yin, S. N. Dong and X. G. Li, *Sci. Rep.*, 2017, **7**, 43540.
28 P. J. Klar and T. Rentschler, *Solid State Commun.*, 1997, **103**, 341–345.
29 X. Hu, W. Wang, X. Mao and X. Chen, *Magnetic and electric properties of co-doped $Bi_5Ti_3FeO_{15}$ multiferroic ceramics*, Chinese Physical Society, 2010, vol. 59, pp. 8160–8107.
30 Q. Li, J. Wang, M. Li, S. Guo, J. Zhang, Z. Hu, Z. Zhou, G. Wang, X. Dong and J. Chu, *Phys. Rev. B*, 2017, **96**, 024101–024110.
31 I. Saitoh and S. Kojima, *Ferroelectrics*, 1998, **217**, 83–89.
32 R. E. Melgarejo, M. S. Tomar, A. Hidalgo and R. S. Katiyar, *Ferroelectrics*, 2010, **269**, 297–302.
33 Y. M. Kim, J. He, M. D. Biegalski, H. Ambaye, V. Lauter, H. M. Christen, S. T. Pantelides, S. J. Pennycook, S. V. Kalinin and A. Y. Borisevich, *Nat. Mater.*, 2012, **11**, 888–894.
34 C. Shao, Y. Lu, D. Wang and Y. Li, *J. Eur. Ceram. Soc.*, 2012, **32**, 3781–3789.